Numerical analysis of forced convection in plate and frame heat exchangers

G. Croce and P. D'Agaro
Università degli Studi di Udine, Dipartimento di Energetica e Macchine, Udine, Italy

Keywords *Finite element, Heat exchangers, Forced convection*

Abstract *A three-dimensional numerical investigation of flow field and heat transfer in sine-wave crossed ducts is presented. Numerical simulations are carried out using a finite element procedure based on an algorithm which shares many features with the SIMPLER finite-volume method, and utilizes equal order pressure–velocity interpolation functions. Since the flow, after a short entrance regime, reaches the fully developed condition, the computational domain can be reduced to a single periodic element and periodic boundary conditions are assumed at the entrance, the exit and the sides. The thermal performance and the frictional pressure losses of the crossed-corrugated plates are investigated for different Reynolds number, from steady up to transitional regimes. The evolution from steady to unsteady flow structure is detected and the influence of the unsteadiness on heat transfer and on pressure drop is analysed. Simulations are performed for both air* ($\mathrm{Pr} = 0.7$) *and water* ($\mathrm{Pr} = 7$) *as the flow medium and the dependence of Nusselt number on Prandtl number is investigated.*

Nomenclature

a = plate corrugation amplitude [m]
A = cross section [m^2]
A' = surface parallel to inflow/outflow boundaries [m^2]
D_H = hydraulic diameter [m]
f = friction factor [no unit]
h = heat transfer coefficient [W/m^2K]
H = channel average height: $H = 2a$
k = thermal conductivity [W/m K]
m = correlation parameter $\mathrm{Nu} = hL/k = f(\mathrm{Re})\cdot\mathrm{Pr}^m$
n = unit vector normal to a surface [no unit]
Nu = Nusselt number [no unit]
p = pressure [Pa]
$\tilde{p}$ = periodic component of pressure [Pa]
Re = Reynolds number [no unit]
t = temperature [°C]
u, v, w = velocity components in the (x, y, z) directions [m/s]
v = velocity vector [m/s]
x, y, z = Cartesian coordinates [m]

Greek

φ = angle between corrugation and main stream flow [°]
α = overall pressure gradient in the flow direction [Pa/m]
λ = wavelength of the corrugation [m]
ν = kinematic viscosity [m^2/s]
ρ = density [kg/m^3]

Subscripts and superscripts

b = bulk
i = inflow
low = lower wall
o = outflow
w = wall
0 = referring to the smooth plane channel
up = upper wall
- = mean value

International Journal of Numerical Methods for Heat & Fluid Flow, Vol. 12 No. 6, 2002, pp. 756-771.

DOI 10.1108/09615530210438382

Introduction

Corrugated plates are the elementary component in plate and frame heat exchangers (PHE) and in compact regenerators and recuperators. In both types of heat exchangers the metal plates are closely packed in a frame so that the orientation of the corrugation between adjacent plates is non-aligned. This configuration improves heat transfer by providing a larger effective surface area and by generating a complex flow structure in the patterns between the plates. Corrugations also strengthen the plates and give a high structural stability due to the multitude of contact points.

Since the corrugation geometry determinates the thermohydraulic performance of the exchanger, a large variety of corrugated profiles has been investigated for many different cross-sections. In this paper, we focus on sinusoidal corrugations, characterised by ratio λ/a between the wavelength λ and the amplitude a of the sinusoid and by the angle φ between the corrugations and the main flow.

In the literature a certain amount of data is available for sine-wave ducts; Okada *et al.* (1972); Focke *et al.* (1985); Gaiser and Kottle (1990) and Ciofalo *et al.* (1996) have experimentally investigated performance of PHE for geometric parameters included in a overall range of $3.5 < \lambda/a < 14.25$ and $0° < \varphi < 90°$.

Analytical solutions, based on the Galerkin integral method, for the velocity and temperature distributions in straight double-sine ducts ($\varphi = 0°$) of different aspect ratios have been presented by Ding *et al.* (1996).

The nature of the fluid flow in the furrows of crossed-corrugated ducts is intrinsically three-dimensional. Therefore a detailed description of the whole flow field is impossible to be obtained by analytical investigations and very difficult to be reached experimentally. Thus, numerical analysis is a very convenient tool to get the complete picture of the complex flow structures over the domain. Furthermore, the flexibility of numerical methods in handling changes in geometric parameters, Reynolds number or boundary conditions helps the comprehension of the mechanisms affecting the flow and temperature fields.

Stasiek *et al.* (1996) used the commercial code Flow3D to solve laminar and turbulent flow equations in a Reynolds number range between 1000 and 10,000. Blomerius *et al.* (1999) and Blomerius and Mitra (2000) carried out parametrical investigations in the laminar and transitional flow regimes in order to detect the onset of self-sustained flow oscillations and to analyse the influence of unsteady flow structure on the heat transfer and pressure loss. A finite volume code developed by the research group was used.

In the reported numerical investigations, the flow medium is air as they refer to the application of the corrugated plates in regenerative and recuperative heat exchangers. However, another main application of crossed-corrugated plates is in chevron form of PHE which is the standard heat transfer equipment for

liquid-food and chemical treatment and is increasingly becoming the standard for closed-circuit cooling applications aboard ships, oil platforms, power station and wherever a close temperature approach is required and weight or space is at a premium (Kumar *et al.*, 1998). In these cases a flow medium with a higher Prandtl number than that of air is involved.

The parameters of the thermal field for fluids other than air are commonly calculated with empirical correlations which identify a polynomial dependence of the Nusselt number on Prandtl number. In this paper, we investigate and compare the temperature fields and the distribution of the heat transfer coefficient over the walls for both air and water.

Most common correlations predict, for a large variety of duct cross sections, the dependence of the Nusselt on $Pr^{1/3}$. In the majority of experimental investigations on PHE the Prandtl exponent has variously taken as 0.5, 0.4 and 0.33 (Okada *et al.*, 1972; Focke *et al.*, 1985 and Muley and Manglik, 1997) related to different geometric factors such as the corrugation profiles and their depth and wavelength. The present computations show a more complex influence, since the actual value of the exponent m is a function of Reynolds numbers.

The flow field and heat transfer are investigated in the laminar flow regime for a geometry characterised by $\varphi = \pm 45°$ and $\lambda/a = 12$ in the Reynolds number range from 100 to 1000 for both air ($Pr = 0.7$) and water ($Pr = 7$). Particular focus has been made on the transition from steady to unsteady flow, investigating how the flow structure affects the performance of the plate heat exchanger.

Numerical simulations are carried out using a finite element procedure described by Nonino and Croce (1997) and Nonino and Comini (1997; 1998). It is based on an algorithm which utilizes an equal-order velocity interpolation for velocity and pressure, and a sequential solution strategy with has features in common with the well-known SIMPLER algorithm.

Statement of the problem

The angle between adjacent plates and between these and the main flow direction (Figure 1(a)) has a decisive influence on the basic flow structure and on the flow patterns. Focke and Knibbe (1986) used an electrode-activated pH method to visualize the flow patterns and concluded that while for inclination angles $|\varphi| > 60°$ the fluid mainly flows along the furrows on each plate, for smaller angles ($|\varphi| < 30°$) the fluid follows the main direction and corrugations introduce only small deviations yielding zig-zag patterns. At $\varphi = \pm 45°$ the two types of trajectories coexist and lead to a highly complex structure that induces the largest swirl generation on the flow in the furrows, the onset of unsteadiness still in laminar flow regime and greater heat transfer enhancement.

Blomerius and Mitra (2000) has identified the geometry with a dimensionless wavelength $\lambda/a = 12$ and a dimensionless channel height $H/a = 2$ as the most

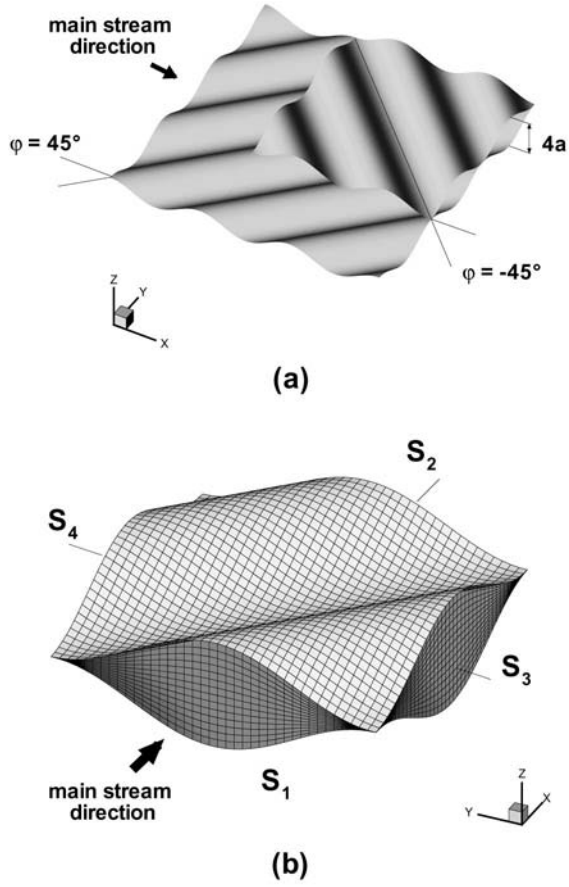

Figure 1.
Sinusoidal cross-corrugated plates geometry. (a) overview φ: inclination angle; a: amplitude of corrugation. (b) computational grid

favourable one in a range of $8 < \lambda/a < 16$ and $1.5 < H/a < 2.5$, on the basis of the performance evaluation criteria of Webb (1981), at least in the two-dimensional configuration ($\varphi = 90°$). In fact it requires less heat transfer area than all other investigated configurations considered under the constraint of constant heat flux, mean flow rate, pumping power and mean temperature difference.

Accounting for these results, we assumed the corresponding three-dimensional configuration with $\varphi = \pm 45°$. The corrugated surfaces are described by the following equations:

$$z_{\text{low}}(x, y) = -a \sin(2\pi/\lambda \cdot (y - \lambda/4)) \tag{1}$$

$$z_{\text{up}}(x, y) = a \sin(2\pi/\lambda \cdot (y - \lambda/4)) + a$$

Computational domain and boundary conditions

Corrugated ducts are characterised by a repetitive geometry in both streamwise and transverse directions. After a short entrance regime, the flow and the thermal fields become fully-developed and repeat themselves from module to module in an identical or similar way. Therefore, it is possible to reduce the numerical analysis to this single periodic element. Boundary conditions are assumed at the entrance S_1, at the exit S_2, and on the sides S_3 and S_4 of the computational domain (Figure 1(b)).

At the boundaries (S_3, S_4) standard periodic boundary conditions are imposed on pressure, velocity and temperature. With incompressible flow hypothesis, periodic boundary conditions can be assumed on the velocity also at the inflow and outflow boundaries and similar conditions are carried out for pressure p and temperature t.

The pressure p can be expressed as the sum of a linear term, accounting for the pressure gradient α in the flow direction x, and a residual periodic term $\tilde{p}$:

$$p = -\alpha x + \tilde{p} \tag{2}$$

The periodicity of $\tilde{p}$ between boundaries S_1 and S_2 produces the following condition (Nonino and Comini, 1998)

$$\tilde{p}_{\mathrm{o}}(y,z) = \tilde{p}_{\mathrm{i}}(y,z) \tag{3}$$

where i and o indicate the inlet and the outlet of the repetitive element.

Boundary conditions on velocity are assumed at the wall boundaries and at the periodic boundaries and no-slip conditions at the wall boundaries

$$u = v = w = 0 \tag{4}$$

and symmetric periodicity between S_1 and S_2

$$\begin{aligned} u_{\mathrm{o}}(y,z) &= u_{\mathrm{i}}(y,z) \\ v_{\mathrm{o}}(y,z) &= v_{\mathrm{i}}(y,z) \\ w_{\mathrm{o}}(y,z) &= w_{\mathrm{i}}(y,z) \end{aligned} \tag{5}$$

Since conditions in equation (5) do not require any specification of the velocities values at the inflow boundary, the pressure gradient α must be repeatedly adjusted until the desired value of the average velocity on the cross-section A is reached:

$$\bar{u} = \frac{1}{A}\int_{\mathrm{A}} u \, \mathrm{d}A \tag{6}$$

A uniform temperature condition is assumed on the walls

$$t = t_{\mathrm{w}} = \mathrm{cost} \tag{7}$$

while the periodicity of thermal field between S_1 and S_2 is imposed on the distribution of the dimensionless temperature T, which identically repeats itself from module to module. It is defined as

$$T = \frac{t - t_w}{t_b - t_w} \tag{8}$$

where t_b is the bulk temperature defined as follows

$$t_b = \frac{\int_{A'} |\mathbf{v}\cdot\mathbf{n}| t \, dA}{\int_{A'} |\mathbf{v}\cdot\mathbf{n}| dA} \tag{9}$$

where A' is the area of a surface parallel to the inflow/outflow boundaries and $\mathbf{n}$ is the unit vector normal to it.

Therefore, the symmetric periodicity of T is expressed by the following condition:

$$\frac{t_o(y,z) - t_w}{(t_b)_o - t_w} = \frac{t_i(y,z) - t_w}{(t_b)_i - t_w} \tag{10}$$

Rearranging equation (10), the following expression is obtained

$$t_o(y,z) = \left[1 + \frac{(t_b)_o - (t_b)_i}{(t_b)_i - t_w}\right] t_i(y,z) - \frac{(t_b)_o - (t_b)_i}{(t_b)_i - t_w} t_w \tag{11}$$

where the T-bulk at inflow $(t_b)_i$ and the difference of the T-bulk at the outflow and inflow are unknown quantities. Therefore, in the solution process, the difference in T-bulk is at first imposed, and then an iterative process is carried on until convergence is reached for the value of $(t_b)_i$ that verifies condition (10).

Numerical solution

In the solution procedure, the momentum, continuity and energy equations are solved by the finite element algorithm described in Nonino and Croce (1997). The velocity–pressure coupling is realized by a method which has many features in common with the SIMPLER algorithm. At each new time step $(n + 1)$, a pseudo-velocity field is obtained by the velocity field at the end of previous time step (n) by neglecting the gradient of pressure periodic component in the momentum equations. Continuity is enforced on the pseudo-velocity field, computing a tentative pressure from the resulting Poisson equation, and the momentum equations are solved for the tentative velocity field. By enforcing continuity again, the pressure corrections are found and used to calculate the velocity corrections and consequently the new velocity

field. Once the velocity field at time step $(n+1)$ has been found, the energy equation can be solved before moving to the next time step.

The momentum, pressure and energy equations are solved in sequence, following a fully segregated approach.

Since the space discretization of each equation is based on the Bubnov–Galerkin method, no upwinding technique is introduced. The application of Green's theorem to the diffusion term of each equation yields the weak form and allow the imposition of Neumann boundary conditions.

Flow field

For most of the computations, the elementary periodic domain has been discretized by a structured grid consisting of $40 \times 40 \times 15$ points (Figure 1(b)). For the Reynolds=1000, a finer grid of $70 \times 70 \times 25$ nodes was required to obtain grid-independent values at both Prandtl values. Using the wave amplitude a as reference length, the dimensionless distance of the first node from the walls varies from 1.43×10^{-4} to 2.85×10^{-1} and from 8.33×10^{-5} to 1.67×10^{-1} in the coarser and finer grid, respectively. The behaviour of the flow is determined by the Reynolds number

$$\mathrm{Re} = \frac{\bar{u} D_{\mathrm{H}}}{\nu} \tag{12}$$

and can be characterised by the friction factor f

$$f = \frac{2 D_{\mathrm{H}} \alpha}{\rho \bar{u}^2} \tag{13}$$

both defined as a function of the hydraulic diameter D_{H} and the average velocity $\bar{u}$.

Calculations have been performed for six Reynolds numbers ranging from 100 to 1000. Two different flow regimes have been observed: steady flow for $\mathrm{Re} < 300$ and unsteady behaviour for $\mathrm{Re} > 300$. For $\mathrm{Re} > 350$ the flow solution becomes time dependent and self-sustained oscillations in the flow quickly lead to a semi-chaotic behaviour. For all the unsteady results the Fourier analysis of the Nusselt number time series shows a complex behaviour, with a power spectrum broadening at higher Re.

The different flow structures for a steady case ($\mathrm{Re} = 100$) and for a transient case ($\mathrm{Re} = 1000$) have been analysed in detail and compared. The streamwise and secondary velocities for both flow regimes are shown in Figure 2. For $\mathrm{Re} = 100$ they show a steady regular flow, and two distinct streams following the furrows between the corrugations of the plates that are easily recognisable in the plot of the secondary velocity. On the contrary, for $\mathrm{Re} = 1000$ the instantaneous flow field is almost chaotic, a considerable mixing occurs and simple flow structures are not easily identifiable. From the three-dimensional pathline maps of Figure 3(a), it is even more evident that at $\mathrm{Re} = 100$ the flow

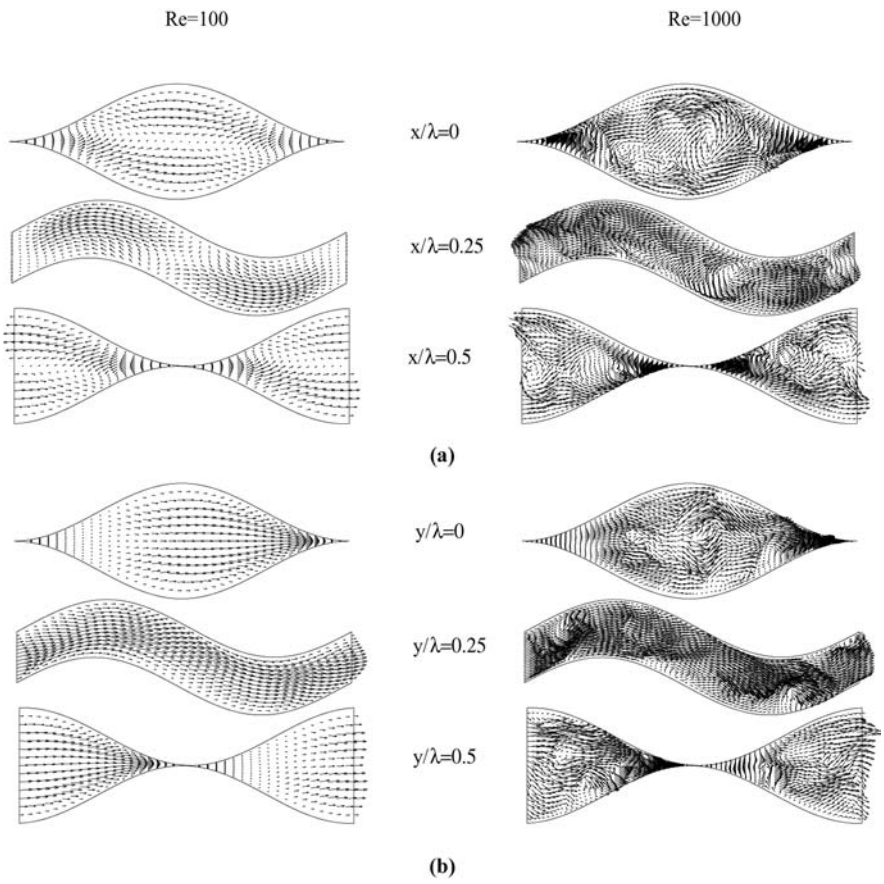

Figure 2.
Velocity vectors.
(a) streamwise velocity,
(b) secondary velocity

mainly follows the valleys of the corrugation of upper and lower walls. The fluid through the inlet cross-section simply splits into two streams: the part under the midplane flows along the valley of the lower plate while the part over the midplane follows the valley of the upper plate. Only a minor part of fluid, in a thin layer between the two major streams, crosses the crests of the corrugations because of the dragging force of a stream on the other. It follows the main flow direction in zig-zag patterns, promoting a little mixing. The flow behaviour, thus, results from the superimposition of two simple channel flows.

On the other hand, at $Re = 1000$ the crest crossing layer is strongly widened, as shown by the time averaged streamlines in Figure 3(b), increasing the flow mixing. Only the fluid very close to the walls follows the corresponding valleys, while all the other streamlines produce criss-crossing interactions along the channel. In order to detect the swirling motions that may be induced by these interactions, the flow field have been analysed on three sequential cross

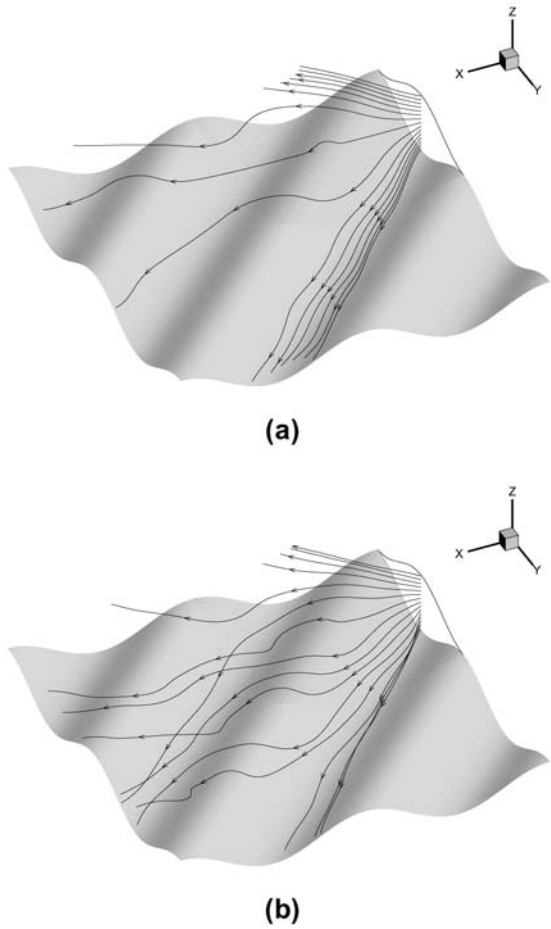

Figure 3.
Streamlines. (a) steady state (Re = 100); (b) transient time averaged case (Re = 1, 000)

sections orthogonal to two adjacent valleys (Figure 4(a)). The plot for the steady case (Figure 4(b)) shows that, while at the bottom of the valley the flow is undisturbed, a small swirl develops by the corrugated profile. Downwards, the section reduces due to the sinusoidal waving of the upper wall and the swirl grows until it occupies the whole channel section. The fluid draws longitudinal vortexes with the axis of rotation aligned with the corrugations. The flow structure is exactly the same in adjacent valleys and it can likewise be referred to the corresponding sections on the upper plate.

The time filtered flow for Re = 1000 (Figure 4) is characterized by a larger vortex that appear in the core of the furrow already in the first cross section, and time-dependent interaction between the furrows occurs. Thus, as can be seen in the central slice Section 2 (Figure 4(c)), two different flow structures

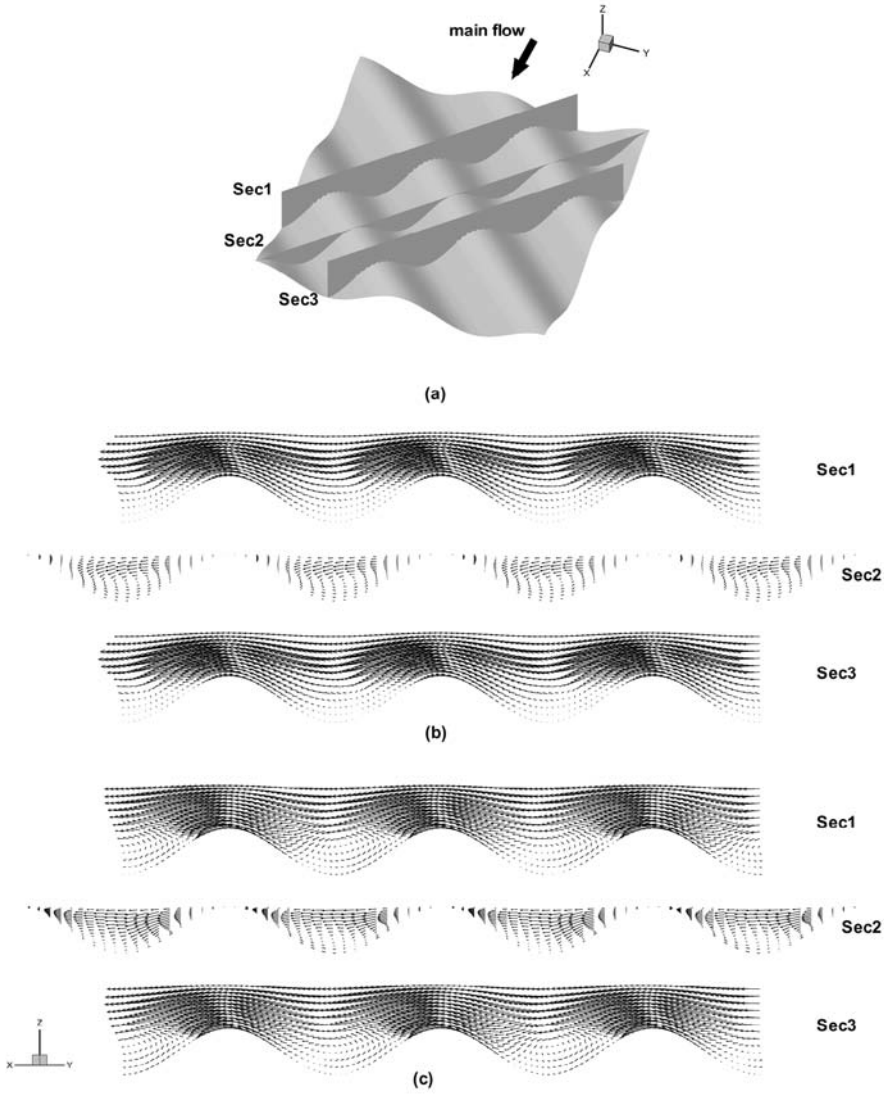

Figure 4.
Sequential cross sections orthogonal to two adjacent valleys. (a) location; velocity vectors for (b) Re = 100 and (c) Re = 1000 time averaged

alternate between adjacent valleys: upper stream drag yields a global motion from right to the left; such flow alternatively generates a bigger longitudinal vortex or deeply penetrates in the furrow.

The transition from steady to unsteady flow implies a considerable increase in friction losses owing to the stronger mixing produced by the interactions between streams of different furrows and by the enlargement of the vortical structures in the valleys themselves. The results in terms of friction factor f are

reported in Figure 5. The reference value f_0 is the friction factor for a fully-developed laminar flow between two straight plates, $f_0 = 24/\mathrm{Re}$. The transition is clearly detected by a significant change in the slope of curves. The transition location is in good agreement with the results of Blomerius and Mitra (2000). Slight deviations from Blomerius data at the beginning of the unsteady region can be due to the uncertainty in the location and description of the transition from the time periodic to semi-chaotic flow.

Temperature field and Prandtl number influence

The calculations for different Re have been performed for water (Pr = 7) and air (Pr = 0.7) as flow medium. Since for incompressible flow the velocity field is decoupled from the thermal one, only the temperature field is affected by the change in Pr.

The mean Nusselt number

$$\mathrm{Nu} = \frac{hD_\mathrm{H}}{k} = f(\mathrm{Re}, \mathrm{Pr}) \tag{14}$$

has been chosen as a significant measure of the overall heat-transfer effectiveness of the heat exchanger.

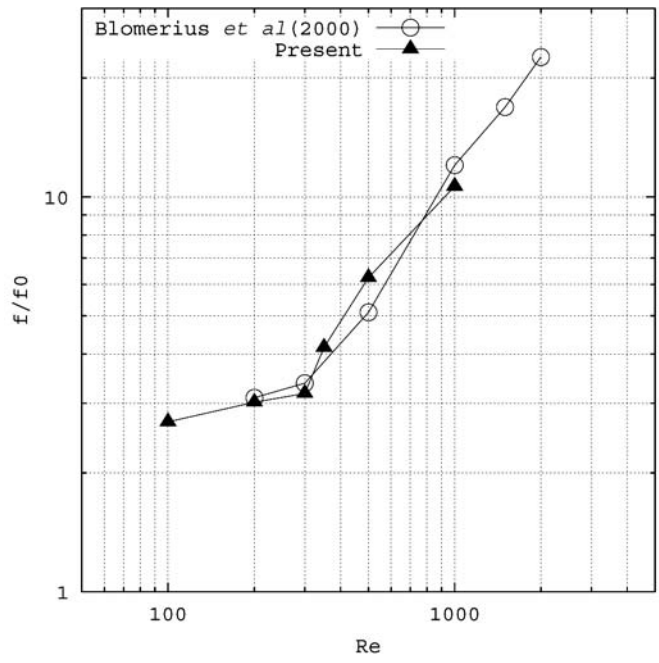

Figure 5.
Friction factor versus Reynolds number

It is interesting to compare the temperature distributions adopting both flow regime and fluid medium as criteria. In Figure 6, temperature distributions for air on the slices parallel to the inlet or to the main flow are plotted in the steady case (Re = 100) and in the transient flow case (Re = 1000). In the first one notes the presence of two stream tubes that are alternatively jointed and split by the geometry of the corrugated plates: at the $x/\lambda = 0$ section they are sharply separated, whereas at the downwash section they merge to be split again by the central narrowing on $x/\lambda = 0.5$ section. On the contrary, for Re = 1000 the mixing and complex interactions of the streams in opposite furrows lead to a much more homogenous temperature distribution over the whole cross section and a consequent heat transfer enhancement.

The temperature field for water is qualitatively similar, but the sharper gradient associated with the reduced thermal diffusivity allows a more clear inspection of the flow structure. As an example, at Re = 100 (Figure 7(a)) we can easily identify the four main streams previously described: the two of them running along the valley bottoms, and two of them crossing the crests and

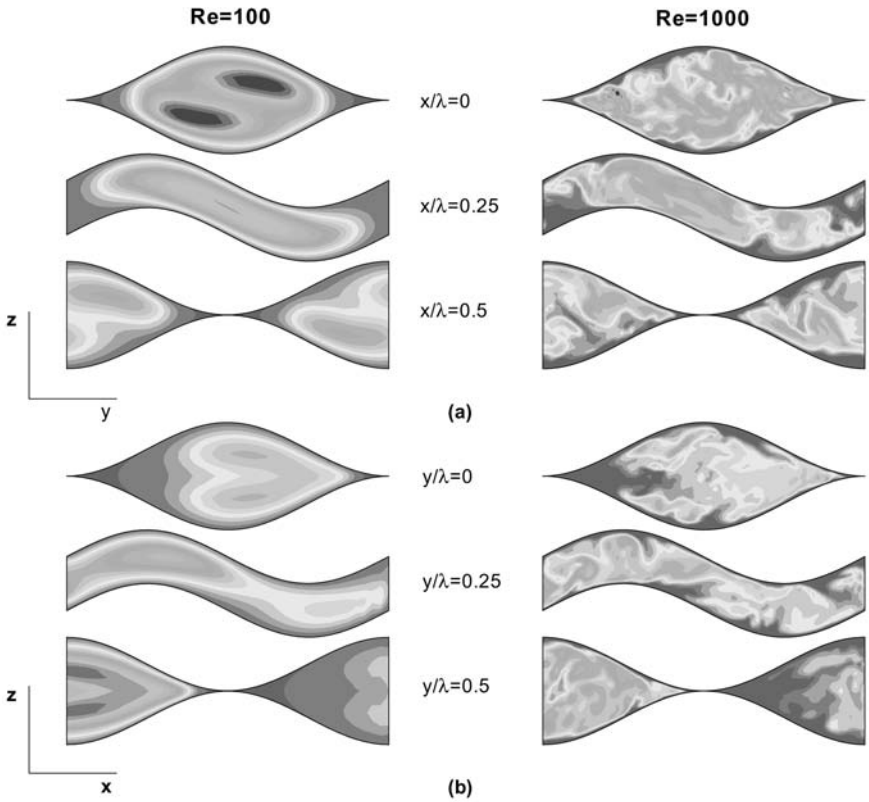

Figure 6.
Temperature fields for air (Pr = 0.7). (a) sections orthogonal to the main flow, (b) sections parallel to the main flow

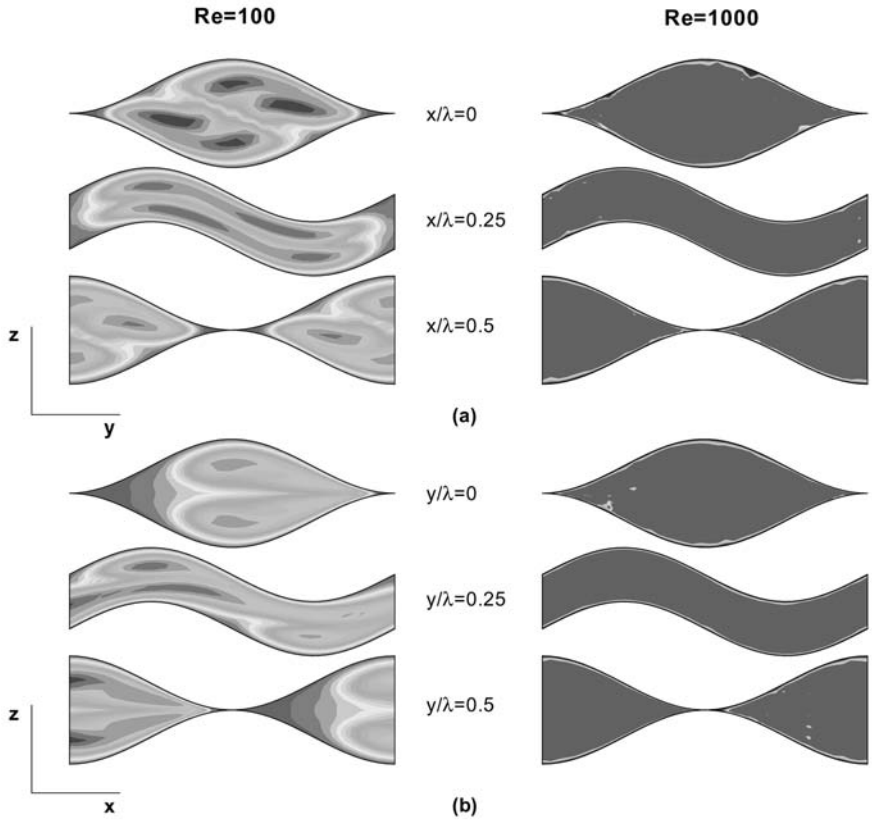

Figure 7.
Temperature fields for water (Pr = 7).
(a) sections orthogonal to the main flow,
(b) sections parallel to the main flow

roughly following the main flow direction with a zig-zag pattern. At Re = 1000 (Figure 7(b)), a nearly uniform core flow temperature is the clear effect of strong mixing.

In analogy with its effect on friction factor, the transition from steady to unsteady flow yields a considerable enhancement in heat transfer. The Nusselt number is plotted as a function of Re in Figure 8. Again, the reference value Nu_0 is the straight plain channel value, $Nu_0 = 7.537$.

As may be expected, the increase in Prandtl number yields an increase in the heat transfer rate, due to the sharpening of temperature gradient. However, the dependence on the Pr value is not obvious, since the flow structure is far from a simple boundary layer-like condition.

Most common correlations report a dependence of the form

$$\mathrm{Nu} = \frac{hD_{\mathrm{H}}}{k} = f(\mathrm{Re})\mathrm{Pr}^{m} \tag{15}$$

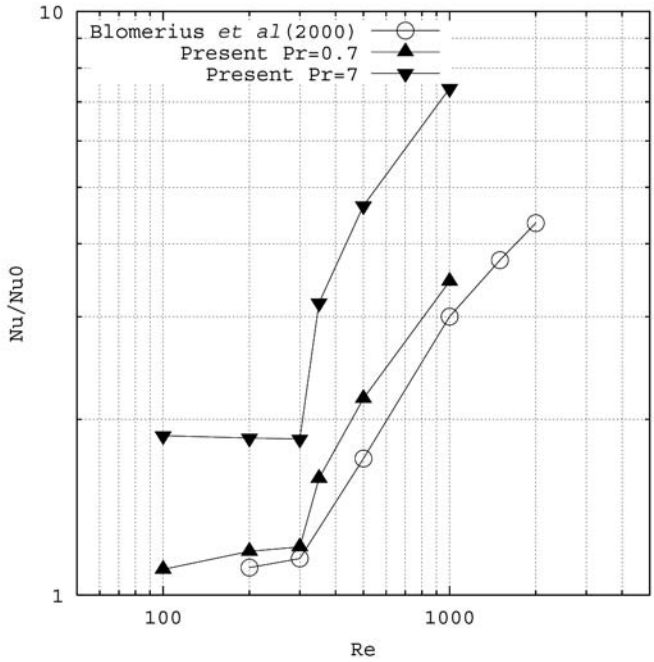

Figure 8.
Nusselt number versus Reynolds number

with m not far from 1/3. However, for a steady laminar flow in a straight duct it is known that Nu is independent of both Re and Pr, yielding a value of $m = 0$. In Figure 9 we plot the actual value of m computed from the present results as

$$m = \frac{\log\left(\frac{\mathrm{Nu_{air}}}{\mathrm{Nu_{water}}}\right)}{\log\left(\frac{\mathrm{Pr_{air}}}{\mathrm{Pr_{water}}}\right)} \tag{16}$$

versus Reynolds number. It appears that at high Re the value of m is not far from the usual value of 1/3, while it is considerably lower at $\mathrm{Re} < 300$ and it has a smooth variation in the region of steady/unsteady transition. Thus, the effect of Pr is more significant for the unsteady regime, characterized by higher heat transfer effectiveness.

Conclusions

A detailed analysis of flow and heat transfer in plate and frame heat exchangers has been carried out for two different operating fluid, air and water. The computations showed two distinct flow regimes, a steady one with a small mixing layer between the lower and upper streams, and an unsteady one, with longitudinal vertical structures leading to strong mixing. As a consequence,

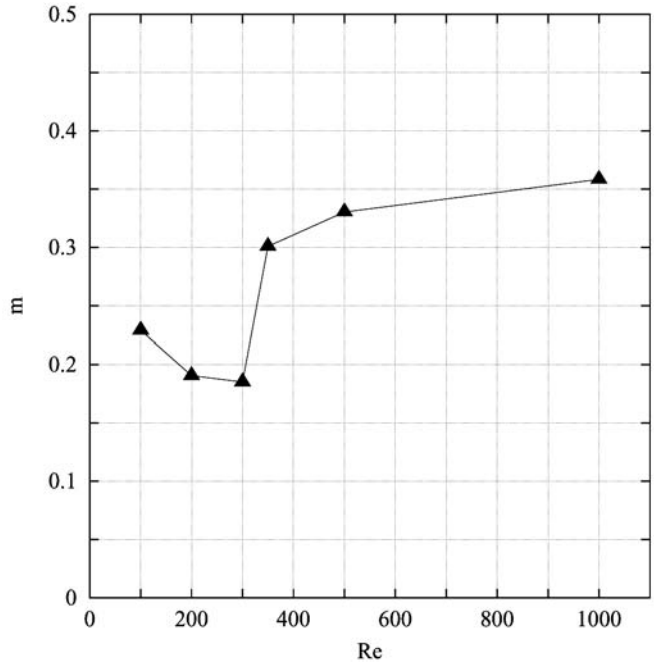

Figure 9.
Plot of value of the exponent m in the correlation between Nu and Pr numbers

relatively small heat transfer enhancement was achieved for low Reynolds numbers, while a dramatic increase in Nusselt number is obtained in the unsteady flow regime, with the drawback of a corresponding increase in friction factor.

The analysis of the influence of the fluid properties shows that it is not possible to identify a single correction factor to take into account the variation of the Prandtl number, thus requiring a numerical evaluation of its effect. The dependence of Nu on Pr is, in fact, a function of Re, and is stronger in the unsteady region, approaching the typical effect observed in turbulent flows.

References

Blomerius, H. and Mitra, N.K. (2000), "Numerical investigation of convective heat transfer and pressure drop in wavy ducts", *Numerical Heat Transfer, Part A*, Vol. 37, pp. 37-54.

Blomerius, H., Holsken, C. and Mitra, N.K. (1999), "Numerical investigation of flow field and heat transfer and in cross-corrugated ducts", *Int. J. Heat Transfer*, Vol. 121, pp. 314-21.

Ciofalo, M., Stasiek, J. and Collins, M.W. (1996), "Investigation of flow and heat transfer in corrugated Passages-II. Numerical simulations", *Int. J. Heat Mass Transfer*, Vol. 4, pp. 165-92.

Comini, G., Del Giudice, S. and Nonino, C. (1994), *Finite Element Analysis in Heat Transfer: Basic Formulation and Linear Problems*, Taylor & Francis, Washington DC.

Focke, W.W. and Knibbe, P.G. (1986), "Flow visualization in parallel plate ducts with corrugated walls", *J. of Fluid Mechanics*, Vol. 165, pp. 73-7.

Focke, W.W., Zachariades, J. and Olivier, I. (1985), "The effect of the corrugation inclination angle on thermohydraulic performance of plate heat exchangers", *Int. J. Heat Mass Transfer*, Vol. 28 No. 8, pp. 1469-79.

Gaiser, G. and Kottle, V. (1990), "Effects of corrugations parameters on local and integral heat transfer in plate heat exchangers and regenerators", *Proc. 9th Int. Heat Transfer Conference*, Jerusalem, Vol. 5, pp. 85-90.

Kumar, H., Cooper, A. and Usher, J.D. (1998), "Plate heat exchangers", in, *Heat Exchanger Design Handbook*, Ch. 3.7. Hewitt, G.F., (Eds) Part 3 Begell House, Inc., New York Wallingford (UK).

Muley, A. and Manglik, R.M. (1997), "Enhanced heat transfer characteristics of single-phase flows in a plate heat exchanger with mixed chevron plates", *J. Enhanched Heat Transfer*, Vol. 4, pp. 187-201.

Nonino, C. and Comini, G. (1997), "An equal-order velocity-pressure algorithm for incompressible thermal flows. Part 1: Formulation", *Numerical Heat Transfer, Part B: Fundamentals*, Vol. 32, pp. 1-16.

Nonino, C. and Comini, G. (1998), "Finite-element analysis of convection problems in spatially periodic domains", *Numerical Heat Transfer, Part B*, Vol. 34, pp. 361-78.

Nonino, C. and Croce, G. (1997), "An equal-order velocity-pressure algorithm for incompressible thermal flows. Part 2: Validation", *Numerical Heat Transfer, Part B: Fundamentals*, Vol. 32, pp. 17-36.

Okada, K., Ono, M., Tominura, T., Okuma, T., Konno, H. and Totani, S. (1972), "Design and heat transfer characteristics of a new plate heat exchangers", *Heat Transfer-Japanese Research*, Vol. 1 No. 1.

Patankar, S.V. (1980), *Numerical Heat Transfer*, Hemisphere, Washington DC.

Stasiek, J., Ciofalo, M., Smith, I.K. and Collins, M.W. (1994), "Experimental and analytical studies of fluid flow and c across corrugated-undulated heat exchangers surfaces", *Proc. 10th Int. Heat Transfer Conference*, Brighton, Vol. 6, pp. 103-9.

Stasiek, J., Collins, M.W., Ciofalo, M. and Chew, P.E. (1996), "Investigation of flow and heat transfer in corrugated Passages-I. Experimental simulations", *Int. J. Heat Mass Transfer*, Vol. 39 No. 1, pp. 149-92.

Webb, R.L. (1981), "Performance evaluation criteria for use of enhanced heat transfer surfaces in heat exchanger design", Vol. 24, pp. 715-26.